Electronic Supplementary Material (ESI) for Lab on a Chip
This journal is © The Royal Society of Chemistry 2012

Electronic Supplementary Information (ESI)

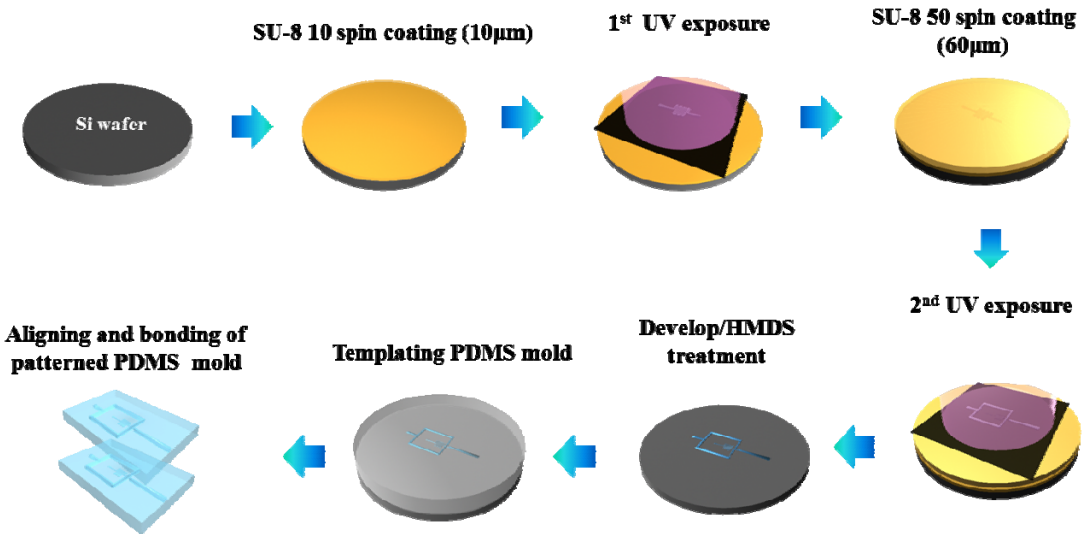

Fig. S1. Schematic illustration of the multi-step lithography process. The SU-8 masters with 3-D topography were fabricated by conventional two-step photolithography procedures. Complementary masters were used to prepare two PDMS microchannels that were mirror image structures of one another, which could be brought together to form a 3-D microchannel device.

This journal is © The Royal Society of Chemistry 2012

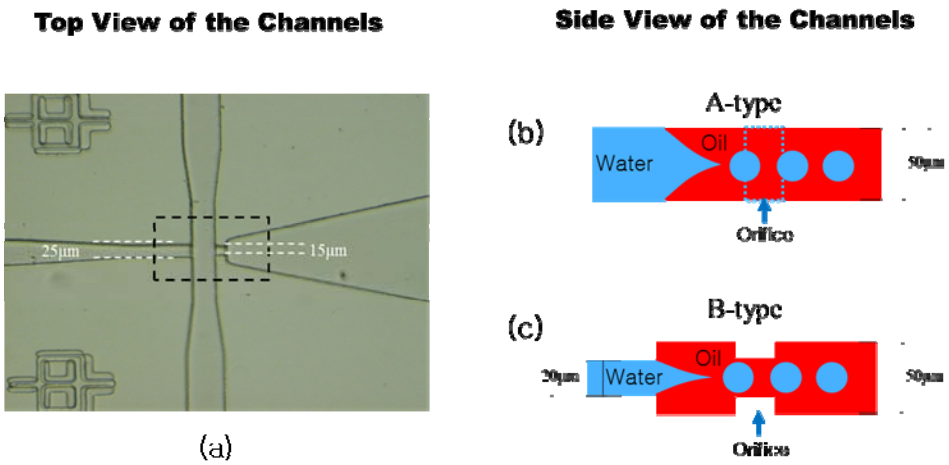

Fig. S2. (a) Top and (b-c) side views for the two different microfluidic flow-focusing devices. (b) A-type: Conventional 2-D geometry which the channel height is uniform throughout the microchannels. (c) B-type: The dispersed phase (water) channel and orifice are lower in height than the continuous (oil) phase and downstream channel.

This journal is © The Royal Society of Chemistry 2012

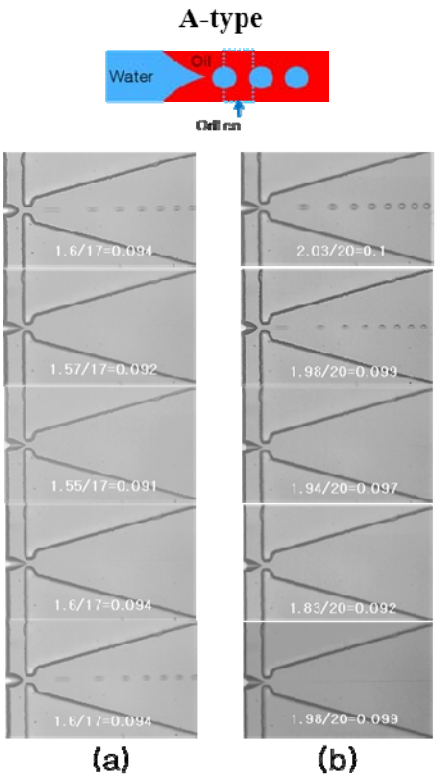

Fig. S3. Representative still images of the droplet breakup processes of the A-type microfluidic flow-focusing device at the indicated pressure ratios (P_w/P_o). The inner fluid was distilled water and the outer fluid was mineral oil containing a 3 wt% silicone-based nonionic surfactant (ABIL EM90). After adjusting the inlet pressures, droplet breakup was allowed to come to equilibrium for several minutes. (a) The tip-streaming phenomenon did not occur until the oil pressure reached to 17 psi. At the pressure ratio (P_w/P_o) of 1.57/17, the visible thread ejected from a highly cusped tip was first observed. However, when the water pressure was decreased to P_w/P_o = 1.55/17, no thread formation was observed. At this moment, we changed our scanning direction and increased the water pressure to see the general feature of the onset of tip-streaming in a wider range of the pressure ratio (P_w/P_o). Indeed, when the pressure ratio P_w/P_o reached to 1.6/17, thicker thread was created in the tip-streaming mode. This behavior was transient and showed the transition to the dripping mode after 3 minutes. (b) At the oil pressure of 20 psi, the visible thread of the tip-streaming mode was observed in the very narrow range between P_w/P_o = 1.96/20 and P_w/P_o = 1.92/20. Again, the increase in water pressure from P_w/P_o = 1.83/20 to P_w/P_o = 1.98/20 created the stable tip-streaming mode without transition to the dripping mode.

This journal is © The Royal Society of Chemistry 2012

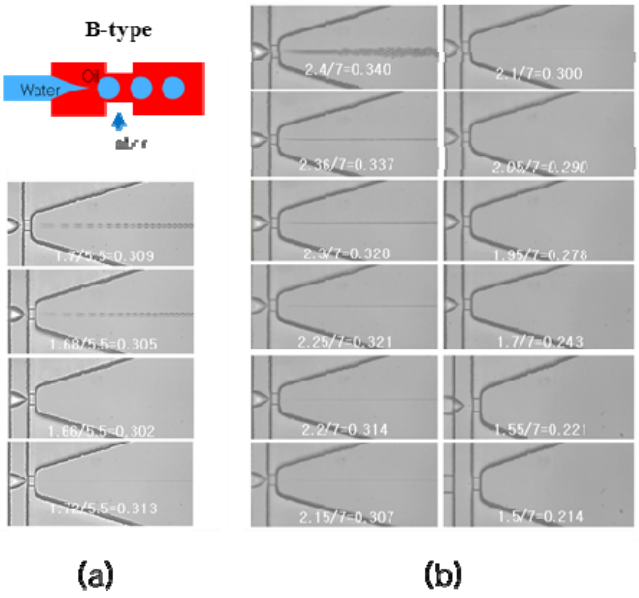

Fig. S4. Representative still images of the droplet breakup processes of the B-type microfluidic flow-focusing device at the indicated pressure ratios (P_w/P_o). Compared with the A-type geometry in Fig. S3, the B-type geometry suggests a fundamental difference in the droplet break-up. A set of images showed that droplet generation in the tip-streaming mode was very stable in a broader range of pressure. (a) The visible tip-streaming thread was first observed by increasing the water pressure from $P_w/P_o = 1.66/5.5$ at which a stagnant conical tip was formed but no thread formation was observed. The increase in the water pressure to $P_w/P_o = 1.72/5.5$ created the stable thread in the tip-streaming mode. (see Movie clip S3) (b) This geometry had the broad tip-streaming range from $P_w/P_o = 2.36/7$ to $P_w/P_o = 1.95/7$. Below the pressure ratio of $P_w/P_o = 1.95/7$, the dispersed phase fluid pressure was too low to penetrate into the orifice after contraction. As the pressure ratio decreased, the conical tip gradually retracted over a wide pressure range due to the increasing effect of the continuous phase flow.

This journal is © The Royal Society of Chemistry 2012

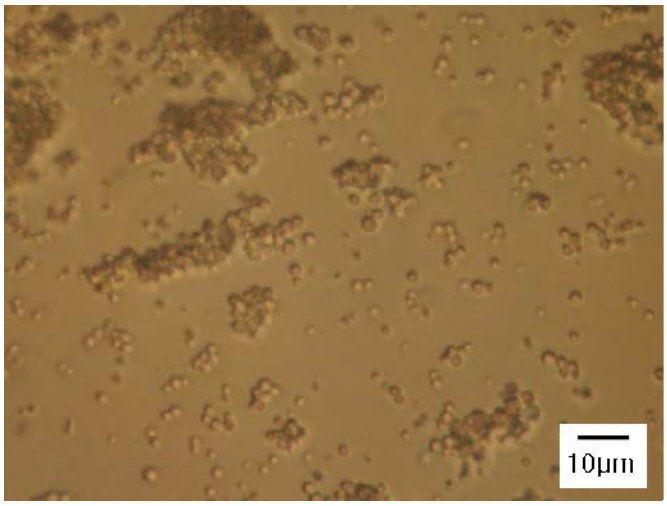

Fig. S5. Optical image of polydisperse water droplets produced from the B-type geometry at 2.3/7 (Pw/Po).

This journal is © The Royal Society of Chemistry 2012

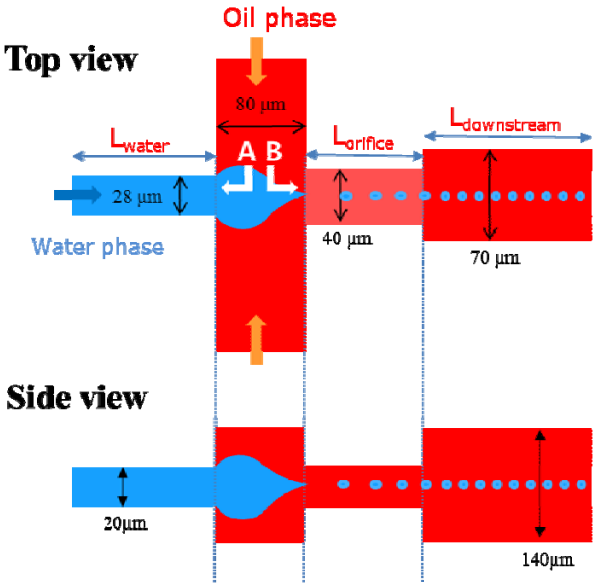

(a)

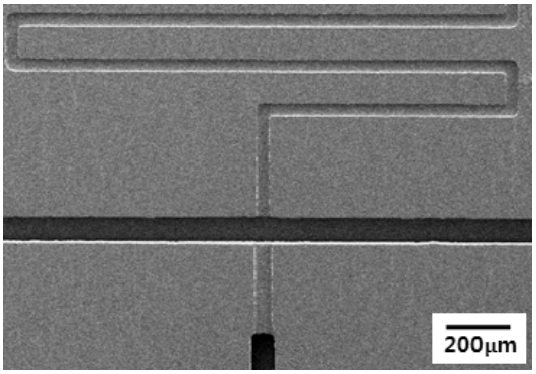

(b)

Fig. S6. (a) The hydraulic resistances in each channel path were calculated using Eq. (1). Here, capillary effects on the water and oil fluids within the hydrophobic PDMS channels were not considered. The hydraulic resistance along path **A (**$R_{water\ channel}$) was 1.53×10^{15} Pa·s/m^3, and the hydraulic resistance along path **B (**= $R_{orifice}$ + $R_{downstream}$) was (7.59×10^{14} + 9.66×10^{12}) Pa·s/m^3. In the case of the flat channels with a constant height (20 μm), the hydraulic resistance in the downstream direction ($R_{downstream}$) was 2.44×10^{15} Pa·s/m^3. (b) SEM image of a PDMS mold prepared from an SU-8 master with 3-D topography. The high-contrast region is 70 μm in height and the low-contrast region is 10 μm in height.

This journal is © The Royal Society of Chemistry 2012

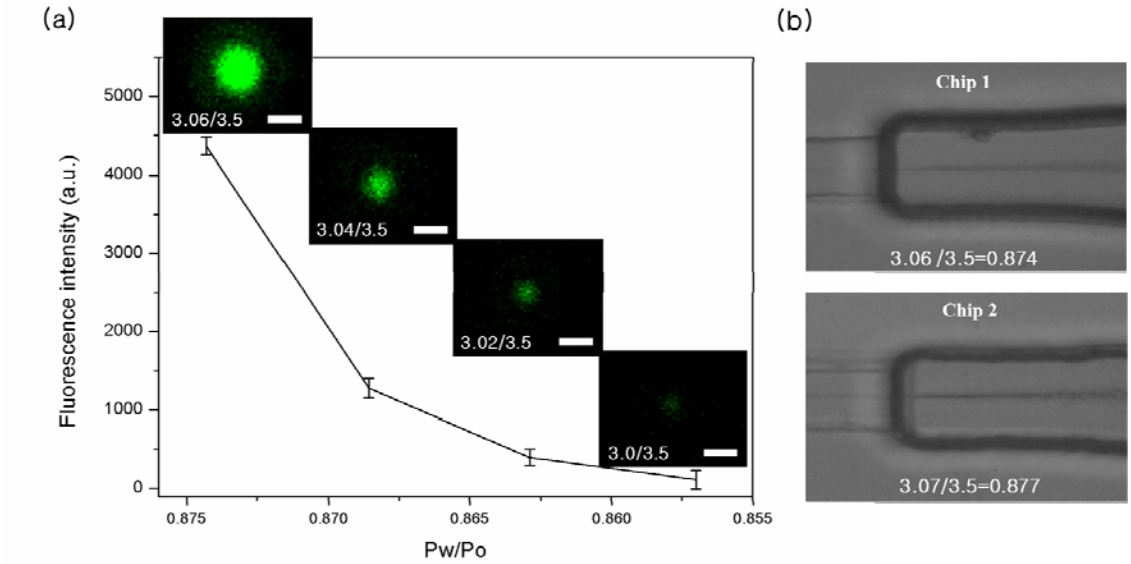

Fig. S7. (a) Representative confocal laser scanning microscopy images of submicron emulsion droplets prepared with Chip 1 at the indicated pressure ratios (P_w/P_o). The scale bars in each image are 1 μm. In order to calculate average fluorescence intensity, we measured the fluorescence intensity of 50 emulsion droplets for each sample. (b) Still images at dripping-to-tipstreaming transition points for chip 1 and 2, respectively. The error from device-to-device variability was as small as 0.01 psi.

This journal is © The Royal Society of Chemistry 2012

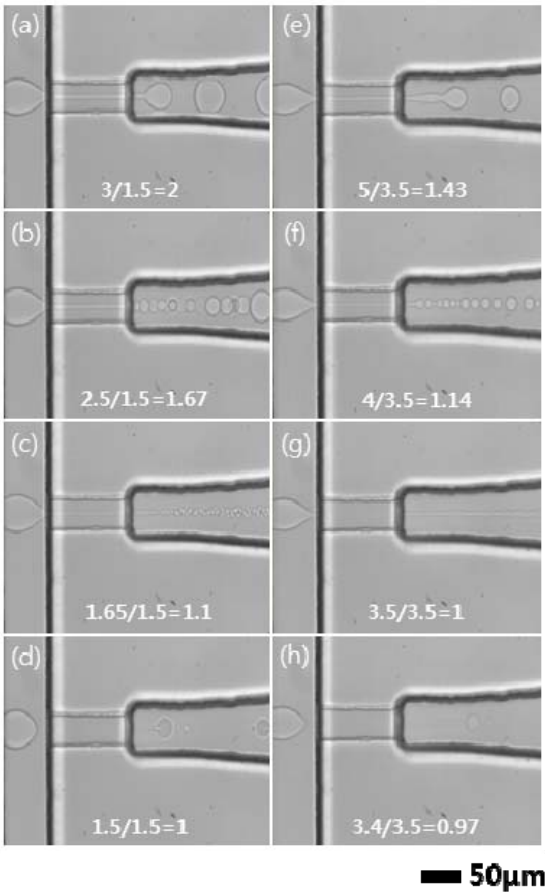

Fig. S8. Representative still images of the droplet breakup processes at the indicated pressure ratios (P_w/P_o), including the (a, e) stable jetting, (b, f) unstable jetting, (c, g) tip-streaming, and (d, h) unstable regime. The inner fluid is PEG-DA (Mn = 700) and the outer fluid is mineral oil containing a 3 wt% silicone-based nonionic surfactant (ABIL EM90). The scale bar is 50 μm at the bottom. Each image presents a close-up view near the orifice, and images are recorded using a high-speed camera at a frame rate of 1 kHz (see Movie clip S2 in Supplementary information).

This journal is © The Royal Society of Chemistry 2012

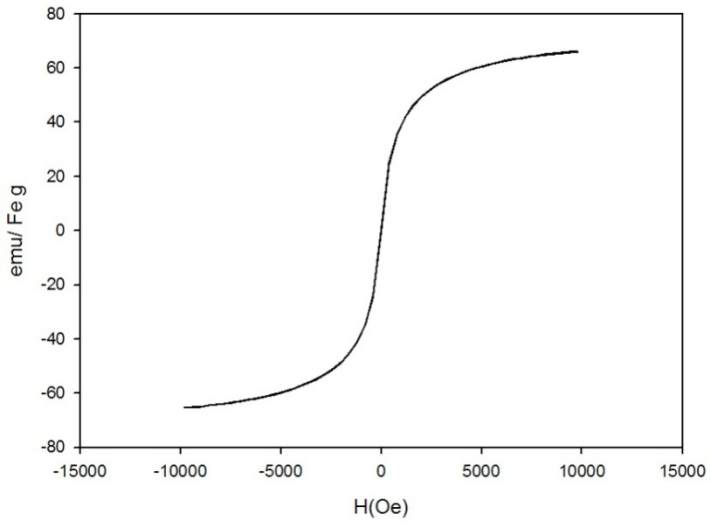

Fig. S9. Magnetization (H) of 8 nm magnetic nanoparticles with hydroxyl groups as a function of magnetic field strength (H), which was measured in vibrating sample magnetometer (VSM).

This journal is © The Royal Society of Chemistry 2012

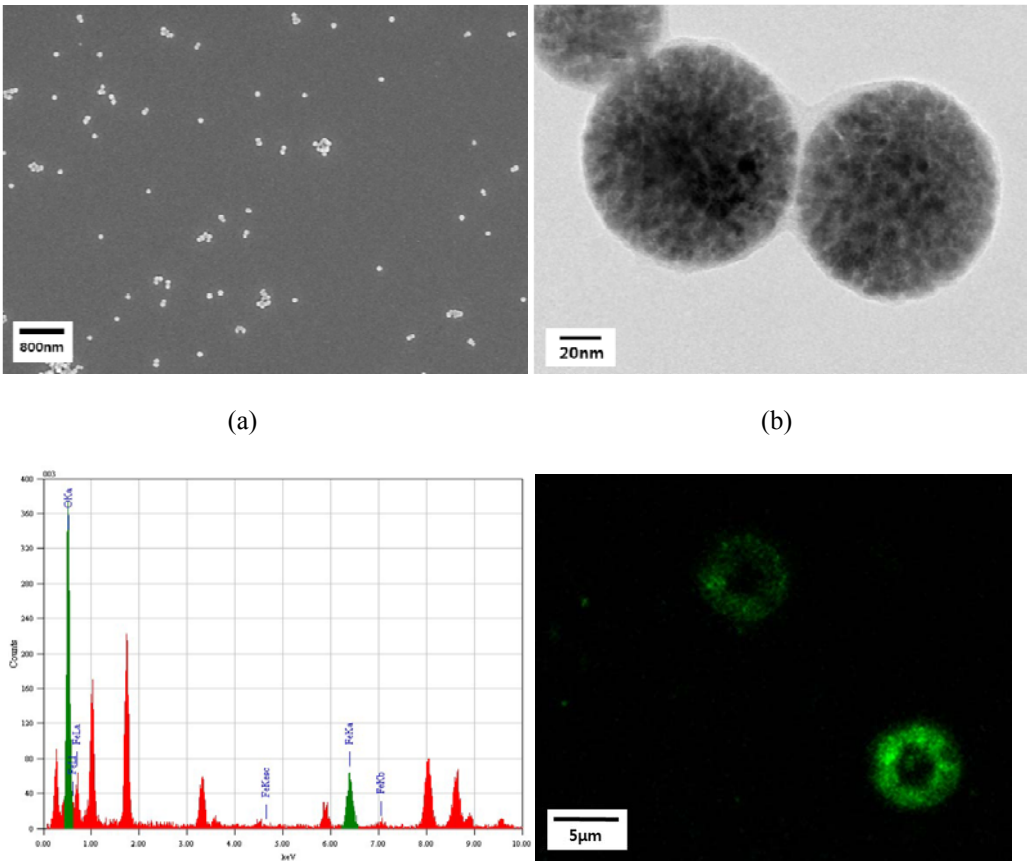

Fig. S10. (a) SEM and (b) TEM images, and (c) energy-dispersive X-ray (EDAX) analysis of composite PEG particles with magnetic nanoparticles, in which size distribution was broad because magnetic nanoparticles with hydroxyl group were not stable in PEG-DA. (d) Confocal laser scanning microscopy image showed core-shell structure of composite PEG particles in mineral oil, in which magnetic nanoparticles were aggregated forming central cores during evaporation and FITC-dextran became shell surrounding cores.